

A New High Parallel-Field Spectrometer at TRIUMF's β -NMR Facility

Edward Thoeng,^{1,2, a)} Ryan M. L. McFadden,^{2,3, b)} Suresh Saminathan,² Gerald D. Morris,² Philipp Kolb,² Ben Matheson,² Md Asaduzzaman,^{2,3} Richard Baartman,² Sarah R. Dunsiger,^{2,4} Derek Fujimoto,^{1,5, c)} Tobias Junginger,^{2,3} Victoria L. Karner,^{5,6, c)} Spencer Kiy,² Ruohong Li,² Monika Stachura,^{2,7} John O. Ticknor,^{5,6} Robert F. Kiefl,^{1,2,5} W. Andrew MacFarlane,^{2,5,6} and Robert E. Laxdal^{2,3, d)}

¹⁾Department of Physics & Astronomy, University of British Columbia, 6224 Agricultural Road, Vancouver, BC V6T 1Z1, Canada

²⁾TRIUMF, 4004 Wesbrook Mall, Vancouver, BC V6T 2A3, Canada

³⁾Department of Physics and Astronomy, University of Victoria, 3800 Finnerty Road, Victoria, BC V8P 5C2, Canada

⁴⁾Department of Physics, Simon Fraser University, 8888 University Drive, Burnaby, BC V5A 1S6, Canada

⁵⁾Stewart Blusson Quantum Matter Institute, University of British Columbia, 2355 East Mall, Vancouver, BC V6T 1Z4, Canada

⁶⁾Department of Chemistry, University of British Columbia, 2036 Main Mall, Vancouver, BC V6T 1Z1, Canada

⁷⁾Department of Chemistry, Simon Fraser University, 8888 University Drive, Burnaby, BC V5A 1S6, Canada

(Dated: 1 December 2022)

A new high field spectrometer has been built to extend the capabilities of the β -detected nuclear magnetic resonance (β -NMR) facility at TRIUMF. This new beamline extension allows β -NMR spectroscopy to be performed with fields up to 200 mT parallel to a sample's surface (perpendicular to the ion beam), allowing depth-resolved studies of local electromagnetic fields with spin polarized probes at a much higher applied magnetic field than previously available in this configuration. The primary motivation and application is to allow studies of superconducting radio frequency (SRF) materials, close to the critical fields of Nb metal, which is extensively used to fabricate SRF cavities. The details of the design considerations and implementation of the ultra-high vacuum (UHV) system, ion optics, beam diagnostics are presented here. Commissioning of the beamline and spectrometer with radioactive ions are also reported here. Future capabilities and applications in other areas are also described.

I. BACKGROUND AND MOTIVATION

Superconducting Nb cavities are the enabling technology behind modern high-power and high-energy linear accelerators (LINACs).^{1,2} Electromagnetic radio frequency (RF) fields are stored in RF cavities and are used to efficiently accelerate charged particle bunches (or beams). To reduce LINAC length, hence cost, the electric accelerating field can be increased, but with a proportional increase in the surface magnetic field (B_{surf}) parallel to the RF cavity wall resulting in heat dissipation. Large oscillating B -fields can result in vortex generation and movement of those vortices generates heat as explained below.

SRF LINAC cavities (commonly made out of elemental Nb metal) need to be operated in the superconducting state below the superconducting transition temperature T_c (~ 9.2 K for Nb), requiring extensive cryogenic infrastructure. SRF cavities can only be operated in the Meissner state when B_{surf} is lower than the field of first vortex penetration (B_{vp}), which for Nb is on the order of 200 mT. In the Meissner state, magnetic fields are screened from the interior of the superconductor and can only penetrate on a nm-scale thin layer (~ 100 nm in Nb) from

the surface, defined by the London penetration depth (λ_L). As magnetic fields are increased further beyond B_{vp} in Nb (a type-II superconductor), a transition from the Meissner state to the vortex state occurs where quantized magnetic fluxes (circulated by vortices of supercurrents) enter the interior of the superconductor. The rapid oscillation of these vortices in the RF fields causes severe heat dissipation resulting in a sharp increase in the surface resistance.³

RF dissipation is contained within this surface layer and its response to the applied B_{surf} has a significant impact on the overall performance of the LINAC. Intensive research at SRF facilities worldwide has also demonstrated that the performance of SRF cavities is very sensitive to (and can be enhanced by) various surface modifications (e.g., vacuum heat treatment,⁴⁻⁷ dilute impurity diffusion,^{8,9} and higher B_{vp} superconductor thin film coatings¹⁰⁻¹³). Theoretical studies postulate that a "dirty" layer on a "clean" substrate (or more complicated layered structures) can help shield the underlayer from the formation of dissipative vortices.^{3,10,14} A deeper understanding of how the Meissner screening deteriorates at B_{surf} close to B_{vp} , as well as how different surface modifications result in a reduced RF dissipation and an enhanced B_{vp} is required to improve cavity performance.

Direct current (DC) magnetic fields applied both perpendicular and parallel to the sample surface have been used as analogues of cavity operating conditions to characterize SRF materials with respect to the field of first flux penetration.¹⁵ Perpendicular fields result in highly non-uniform surface fields

^{a)}E-mail: ethoeng@triumf.ca

^{b)}E-mail: rmlm@triumf.ca

^{c)}Current address: TRIUMF, 4004 Wesbrook Mall, Vancouver, BC V6T 2A3, Canada

^{d)}E-mail: lax@triumf.ca

when the sample is in the Meissner state, with flux accentuated at sample edges. Parallel fields on coin shaped or ellipsoid samples provide near uniform surface fields up to the field of first flux penetration. Measurements typically record the maximum local surface field (based on the applied field and the sample geometry) that can be reached before flux is detected in the bulk. Such measurements do not provide local details of the role of the surface layer(s) in the field of first flux entry. Given the interest in layered structures and their precise role in enhancing the field of first flux entry, a diagnostic that provides the depth-resolved information of field attenuation through the London layer would provide new insight.

Useful tools to study SRF materials are techniques utilizing spin-polarized radioactive probes such as the positive muon (μ^+) or radioactive ^8Li ions. In either case, the projectile is implanted into the bulk or near surface where the probe's spin reorients according to the static (i.e., time-average) and dynamic (i.e., stochastic) components of the local magnetic field. The β -decay emissions of the probe are correlated with its spin orientation at the time of decay and the time evolution of the asymmetry of the β -decay provides information about the local magnetic field. Early studies of SRF Nb samples utilized the muon spin rotation (μSR) facility at TRIUMF where magnetic fields were applied perpendicular to the face of the coin shaped samples of SRF material to characterize the field of first flux entry.¹⁶ Later, a spectrometer allowing the application of parallel fields was added¹⁷ and a number of measurements were performed both with ellipsoid and coin samples to characterize the role of various treatments on the field of first flux entry.¹⁵ The low-energy muon spin rotation (LE- μSR) facility at Paul Scherrer Institute (PSI) has a much lower energy muon beam that allows depth-resolved studies in parallel fields.^{18–20} The low momentum muon projectile, however, is easily deflected by the applied parallel field on the sample and is limited to ≤ 30 mT.

TRIUMF's implementation of the β -NMR technique^{21,22} utilizes low-energy ($E \sim 20\text{--}30$ keV) radioactive ions like $^8\text{Li}^+$ that can be spin-polarized in-flight before delivery to a dedicated spectrometer. Like LE- μSR , the β -NMR technique can be used to “soft-land” the ion at the near surface using a sample biased at high voltage (HV). The variable HV bias is used to decelerate the ion to energies varying from hundreds of eV to the full ion energy which in turn allows depth-resolved studies of the local magnetic field. The TRIUMF β -NMR facility^{23,24} is capable of studying samples in high perpendicular field (up to 9 T) or (prior to this work) in parallel fields up to a maximum ~ 24 mT. Compared to low energy muons, the transverse deflection of the radioactive ion beam (RIB) can be more easily compensated and therefore an upgrade of the TRIUMF parallel field capability was proposed and realized. The new facility provides ion deceleration (for depth-resolved studies) at high parallel fields up to 200 mT — a capability unique in the world. This paper describes the new facility, including the design considerations, the installed equipment, and the commissioning with both stable and radioactive beams.

II. β -NMR TECHNIQUE AND THE EXISTING FACILITY AT TRIUMF

β -NMR is a type of nuclear magnetic resonance (NMR) technique which utilizes implanted spin-polarized radioactive nuclei as probes. The main difference compared with conventional NMR is the method of detection. The local field can be monitored using the anisotropic emission of the β -particles (typically MeV energy), which is highly correlated with the direction of the nuclear spin at the time of the decay.

High energy β s are detected in two opposing simple detector telescopes (with pairs of scintillators in coincidence), oriented at 0 and π radians relative to the direction of the initial spin polarization. Due to the parity violation of the β -decay, the β counts per unit time C_0 and C_π differ by a factor proportional to the angular emission probability $W(\theta)$, i.e.,

$$C_\theta(t) = \frac{1}{2} \frac{N(t)}{\tau} W(\theta) = \frac{1}{2} \frac{N(t)}{\tau} \begin{cases} \{1 + A_0 P(t)\} & \text{for } \theta = 0, \\ \{1 - A_0 P(t)\} & \text{for } \theta = \pi, \end{cases} \quad (1)$$

where the total number of nuclei (with mean lifetime τ) present at time t after the beam has turned on and implanted at a constant rate R_0 , is defined as:

$$N(t) = \int_0^t N(t, t') dt' = R_0 \int_0^t \exp[-(t - t')/\tau] dt'. \quad (2)$$

For the remaining terms in eq. 1, A_0 is the proportionality constant which depends on both the properties (solid angle) of the detectors, (β energy-dependent) detection efficiency, and the intrinsic asymmetry A ($A_0 \sim 0.1$ for ^8Li).²¹ $P(t)$ in eq. 1 is the degree of spin-polarization. The count rates are combined to generate the experimental asymmetry:

$$A(t) \equiv \frac{C_0(t) - C_\pi(t)}{C_0(t) + C_\pi(t)} = A_0 P(t), \quad (3)$$

which is directly proportional to $P(t)$. The time evolution of the (longitudinal) spin-polarization can therefore be measured as the probe spin interacts with the local magnetic field inside the sample. This method of detection allows about ten orders of magnitude higher sensitivity (per nuclear spin) than conventional NMR, allowing for the study of situations that are either extremely difficult or impossible with conventional approaches (e.g., thin films, ultra-dilute impurities, etc.).^{21–23}

The implantation energy of β -NMR probes can be varied (e.g., from ~ 0.5 keV to ~ 30 keV) to study the surface of materials on the nm-scale and in a depth-resolved manner. Similar to μSR , the β -NMR technique does not rely on the presence of a suitable NMR nucleus in the material and can therefore be applied to any material at any applied magnetic field (including zero field). In contrast to LE- μSR , where the radioactive lifetime (τ) is 2.2 μs , typical β -NMR probes have a much longer τ (e.g., $\tau = 1.21$ s for ^8Li).²⁵ It is therefore more sensitive to dynamics on a much longer timescale, making the two techniques complementary (rather than competitive). Furthermore, β -NMR ions at TRIUMF need to be spin-polarized in-flight via

optical pumping, whereas surface μ^+ s produced from two-body pion decay are nearly 100% spin-polarized.

The β -NMR technique as implemented at TRIUMF requires a dedicated facility to produce high intensity RIBs with a high degree of spin polarization. In the case of TRIUMF, the high intensity RIBs are produced at the Isotope Separator and Accelerator (ISAC) facility, which uses a 500 MeV cyclotron as a driver to bombard a solid (radio)isotope production target with proton beams.²⁶ The resulting short-lived nuclides are then ionized, extracted, and separated on-line (i.e., using the so-called ISOL method) to produce isotopically pure RIBs before being sent downstream for various experiments. $^8\text{Li}^+$ beams with an intensity of $\sim 10^7 \text{ s}^{-1}$ are routinely available.

Prior to being delivered to the β -NMR end-station, the RIBs at ISAC are spin polarized in-flight using dedicated facility infrastructure (allowing for routine operation) via collinear optical pumping with a circularly polarized resonant laser.²⁷ This step produces $\sim 70\%$ nuclear spin polarization.²⁸ The TRIUMF β -NMR facility has two beamlines: the β -NMR leg, which allows for measurements at high perpendicular fields up to 9 T, and the β -detected nuclear quadrupole resonance (β -NQR) leg, which allows samples to be studied in parallel fields up to ~ 24 mT (prior to this work). The NQR technique is a zero field analogue of NMR that depends on the quadrupole interaction of nuclear spins $> 1/2$ in solids. The spin-polarized RIB can be sent alternately to either of the two beamlines thanks to an electrostatic “kicker” that is used to “pulse” the beam. In this way two experiments can run simultaneously.

At the end of each leg is a spectrometer assembly for sample measurements, containing the detectors, cold finger cryostat (for low temperature measurements), magnets, RF coil, HV deceleration (HV cage and deceleration electrodes), and charge-coupled device (CCD) imaging system. In addition, in order to achieve depth-profiling the sample ladder and cryostat are raised to the bias of the HV platform, which can be varied in order to decelerate the ion beam as it approaches the sample. The bias capability spans from 0-35 kV via a high stability (FuG Elektronik GmbH model HCL) DC power supply. A high voltage interlocked cage surrounds the biased equipment on a platform above the beamline (see the inset of fig. 1).

The β -NMR beamline with high (perpendicular-to-sample-surface) field spectrometer uses a superconducting solenoid to generate fields up to 9 T. The detectors are oriented forward and backward relative to the sample, and the emitted β -particles penetrate through the sample to reach the front detector located downstream of the sample. The back detector, located outside the HV platform, contains a small aperture to allow passage of the RIB. On the β -NQR beamline, the (parallel-field) spectrometer uses a normal conducting Helmholtz coil. The detectors are oriented to the left and right side of the sample, and up to four samples can be loaded simultaneously into the ultra-high vacuum (UHV) chamber via a sample ladder load-lock system. This paper reports the upgrade of the β -NQR leg with the addition of a 1m long extension of the beamline to include a parallel field spectrometer capable of up to 200 mT for unique depth-resolved studies of SRF and other materials.

III. HIGH-PARALLEL-FIELD UPGRADE

The high-parallel-field upgrade on the β -NQR leg was completed in two phases. The scope of phase I was to modify and improve the existing low-parallel-field section. In phase II, an additional ~ 1.02 m of new beamline was installed. Phase I and phase II were completed in June 2019 and in July 2021, respectively.

A. Ion optics

There are three main elements of ion optics used along the β -NQR beamline: electrostatic steerers, electrostatic quadrupoles, as well as a magnetic Helmholtz coil. The steerers compensate for the vertical deflection of the ions as they pass through the fringe of the applied magnetic field and deflect the beam onto the sample; the quadrupoles are used to control the beam shape during transport and to focus the ions onto the sample; and the Helmholtz coil provides the magnetic field on the sample parallel to the surface. An additional four-sector electrode close to the sample (within ~ 50 mm) acts as a deceleration electrode, and allows independent horizontal and vertical steering which is used to compensate for the beam deflection and to re-center the beam on the sample. The layout of the ion optics and Helmholtz coil in the β -NQR leg are shown in fig. 2. There are 3 horizontal steerers (XCB) and 4 vertical steerers (YCB) and two sets of electrostatic quadrupole triplets.

Fig. 2 also shows a model of the new beam line extension complete with a model beam trajectory for the case where the Helmholtz coil is producing 200 mT at the sample. The magnetic fringe field diverts the beam ~ 2.4 cm off-axis through a set of “skimmers”, a vertical steerer, and a thermal radiation baffle. The vertical steerers adjust the position of the beam on the sample, while the radiation shield is used to reduce the heat load on the cryogenically cooled sample. Even though the design was focused on an applied field of 200 mT, the two vertical deflectors can be operated independently to achieve the desired beam path at lower fields (all the way down to zero-field).

Beam focusing is achieved using two sets of quadrupole triplets to obtain an axially symmetric beam on sample. Previously, an Einzel lens was used to focus the beam on the low-parallel-field (sample 1) spectrometer. With the phase I upgrade, the first triplet replaced this Einzel lens and is now used to either obtain an optimum focus on the low-parallel-field spectrometer or can be used in tandem with the second triplet to provide a variable symmetric spot size at the second sample position (sample 2). The optimal setpoints for both triplets can be obtained using the TRANSOPTR code^{30,31} via a web application called *Envelope* (see fig. 3), which is hosted on a local server at TRIUMF.

Several HV power supply modules providing bias to the electrostatic ion optics are installed in two separate crates. Both crates and all the plug-in modules were purchased from WIENER Plein & Baus, Corp., with the first crate (8U or 8 standard rack unit, corresponding to 14" in height) installed in a 19" rack at the beamline level, and the second smaller crate

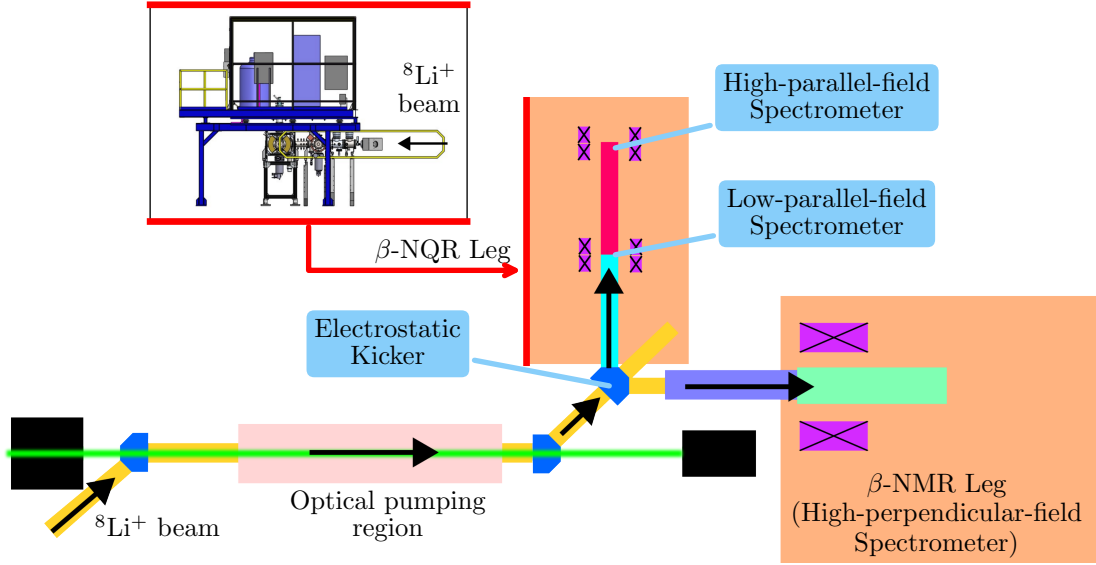


FIG. 1. Beamline layout of the upgraded β -NMR facility. Typical beam energy extracted from the source for $^8\text{Li}^+$ is ~ 20 - 30 keV. The RIB is spin-polarized in-flight (first neutralized with an alkali vapour cell, and later re-ionized by a He vapour cell) using dedicated optical pumping infrastructure, allowing for routine operation. The fast electrostatic kicker allows for semi-simultaneous operation of two spectrometers (i.e., two experiments running at the same time off of a single RIB). At the β -NMR leg, a spectrometer equipped with UHV cold-finger cryostat and superconducting solenoid allows measurements at high magnetic fields (0.5-9 T) perpendicular to the sample surface. The upgraded β -NQR leg provides a new spectrometer for measurements up to 200 mT parallel to the sample surface, just downstream of the existing low-parallel-field (0-24 mT) one. The β -NQR spectrometer is also equipped with a UHV cold-finger cryostat. The inset shows the side view of the upgraded β -NQR beamline and the HV platform above the beamline.

(3U or 5.25" in height) installed in another 19" rack inside the HV platform. The larger crate on the beamline level houses five modules for the β -NQR leg ion optics requiring HV bias relative to ground, and the smaller crate housing two modules is used exclusively for the four-sector electrode biased relative to the HV platform.

For the larger crate, one bipolar module uses 10 HV channels to provide up to ± 500 V for the three horizontal steerers and the first two vertical steerers. Three additional unipolar modules provide six positive and six negative channels with biases up to 6 kV for the two quadrupole triplets. All quadrupole electrodes with the same polarity are wired in parallel with UHV compatible stripped, bare Cu wires, as shown in fig. 4. Not shown are the HV feedthroughs installed in the external vacuum chamber with center conductors that connect to the internal HV wires and electrodes (see also details in fig. 2). One unipolar module (with 8 positive and 8 negative channels) uses 2 pairs of HV positive and negative channels to provide up to 3 kV for each electrode of the last two vertical steerers, which is used to deflect the beam through the thermal radiation baffles. Polarity reversal of this module is achieved with a switch. All beamline devices are remotely operated via an Experimental Physics and Industrial Control System (EPICS)^{32,33} interface.

B. Beam Diagnostics and Beam Tuning

Beam diagnostics are available at discrete locations to aid with the beam tuning via measurements of both the beam current and the beam profile (see fig. 2). The beam current can be measured using three Faraday cups (FCs). The FCs are driven by stepper motor actuators to allow precise positioning with respect to the beam trajectory. All the FCs are typically biased between 60-350 V with either negative or positive polarity, to either trap secondary electrons (i.e., for an absolute current reading) or to amplify the beam intensity during operation (e.g., when using a low-intensity RIB). The driven position of the first two FCs are aligned with the beamline center while the third FC is positioned off-axis (from the beamline center) to allow maximum collection when the beam path follows the reference trajectory. The reference values for the optimum motor positions were obtained by measuring the alignment of the FCs using a theodolite via direct line-of-sight for the case where the Helmholtz coil is producing 200 mT at the sample, during beamline installation.

The beam profile at the sample location is obtained using a CCD camera (Starlight Xpress) mounted on a viewport, by imaging the light emitted by a scintillator (typically sapphire³⁴) on the sample ladder. Imaging of the beam at the sample location is virtually limited to RIB as it is primarily the decay products and not the kinetic energy of the beam that induces scintillation (the β s and α s produced during radioactive decay

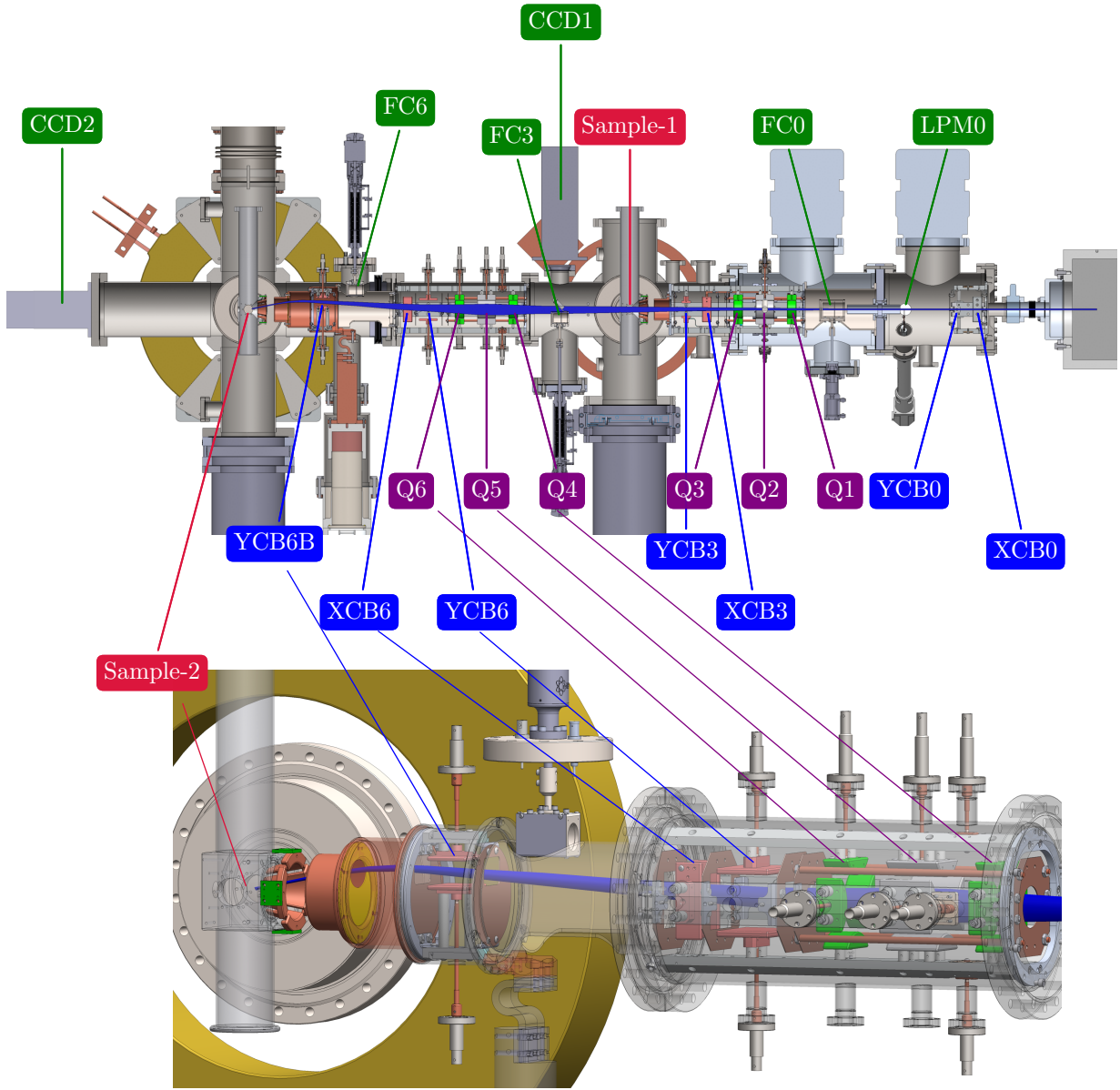


FIG. 2. Details of the upgraded β -NQR leg (see also fig. 1). Top: The final straight section of the beamline (XCB and YCB refer to horizontal and vertical steerers, FC to Faraday cups, Q to quadrupoles, LPM to Linear Profile Monitor). Bottom: Enlarged view of the new beam line extension model, showing the electrostatic quadrupoles, steerers, “skimmer” plates (grounded electrodes with a defined aperture to limit the effective length of optical element), Faraday cup, thermal radiation baffle and final quadrant decelerating electrode. A representative beam trajectory (blue envelope), obtained using a particle tracking code (General Particle Tracer²⁹) for a 200 mT applied field is illustrated in the model.

are in the MeV range, $\sim 10^3$ times more energetic than the beam itself). The beam profile (and centroid position) can also be measured using horizontal and vertical slits driven at 45° in combination with a downstream FC, the so-called linear position monitor (LPM). The LPM plate includes two slits (horizontal and vertical with respect to the beam axis) and three circular collimators of different diameters (8.0 mm, 5.6 mm, and 4.0 mm) on a copper block that allows beam size and position definition for reproducible tuning. The LPM is driven by a stepper motor, with the center of each slit or collimator

(and corresponding stepper motor position) determined during the installation using a theodolite.

The tuning strategy and use of the diagnostics is as follows. The quadrupole triplets are set to theoretical values (from the *Envelope* web application) for a given beam energy and desired spot size. The vertical steerers are set to the theoretical value for the chosen Helmholtz coil setting (i.e., applied field). The beam is first centered on axis and aligned using the LPM0 aperture and downstream FCs. A pilot beam using a stable isotope (e.g., $^7\text{Li}^+$) is often used to establish the trajectory with

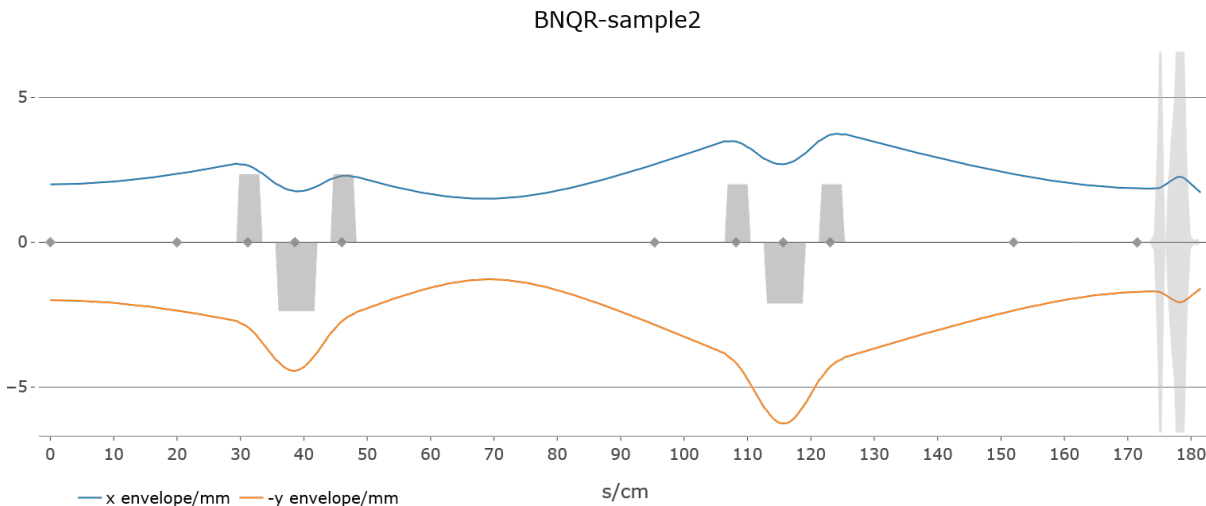


FIG. 3. Plot of the beamline envelope (beam going from left to right) obtained from the *Envelope* calculator based on the TRANSOPTR code,^{30,31} used to tune the beam dimensions under flexible operating conditions via two quadrupole triplets (i.e., for various beamspot sizes, beam energies, HV platform biases, etc). The high-parallel-field and low-parallel-field spectrometer samples are located at 181.5 cm and 76 cm away from the LPM0 (at 0 cm), respectively. The amplitude of the shaded areas located around 39 cm, 115 cm, and 180 cm indicate the focal strength of the first quadrupole triplet, second quadrupole triplet, and HV bias, respectively.

the aid of the 25 mm diameter FCs. Fine tuning of beam spot size and position, particularly at reduced energies, is achieved with direct beam spot imaging using a scintillator (sapphire³⁴) and a CCD camera which views the sample ladder through a glass viewport from the downstream side. The sapphire produces a bright image under irradiation by a RIB, even at the typical low beam intensity for RIBs of 10^6 ions per second. Another scintillator material (YAP:Ce, Proteus, Inc.) has also been used to image stable beam (e.g., during beam development using a non-radioactive ion source) but with a much duller image even at $5 \mu\text{A}$.

C. Ultra-high Vacuum System

Ultra-high vacuum ($\sim 10^{-10}$ Torr) is essential to extend the lifetime of the clean surface of any sample under investigation, particularly during measurements at cryogenic temperatures, to prevent condensation of residual gases. The UHV throughout the beamline is established by differential pumping using a single backing-pump and two turbo-pumps, which can provide pressures down to $\sim 10^{-9}$ Torr. Somewhat lower pressures at the two sample locations are achieved using two separate cryopumps, mounted directly below the sample cryostat, providing base pressures down to $\sim 10^{-11}$ Torr.

The new high-parallel-field spectrometer is built on a stainless steel six-way cross with ConFlat (CF) flanges on each arm. The diameter of the tube along the beam axis is 6" outer diameter (OD), which is a compromise between reasonable pumping speed and a more compact Helmholtz magnet. The top port consists of an 8" CF flange that provides access for the cryostat to be lowered into the beamline. The side ports are 10" CF flanges on 8" OD tube stubs, onto which re-entrant ports with welded thin (0.05 mm) stainless windows are bolted. This

window allows a large diameter space for mounting scintillation detectors within 6.35 cm (2.5") of the sample.

The three existing UHV chambers on the low-parallel-field section have been modified to accommodate the new quadrupole triplet, the LPM, as well as the new FC and viewport for the CCD camera. Two additional vacuum chambers are also fabricated in-house for the beamline extension, which includes one six-way cross for the spectrometer chamber and one beamtube for the upstream steerers and quadrupoles. All UHV chambers are electropolished after tungsten inert gas (TIG) welding and machining. Subsequently, the chambers are leak-checked, and measured with a residual gas analyzer (RGA) after beamline assembly and pump-down.

D. Sample Environment

Magnet Coils

A copper conductor Helmholtz coil is used to provide a magnetic field of up to 200 mT at the sample position. A field uniformity better than 0.01 % is required for β -NMR experiment across a typical beamspot size, full width at half maximum (FWHM) of ~ 3 -4 mm. The number of turns for each coil along the width and height is 8×12 , respectively, producing 56,080 A-turns at a current of 584 A. The coil conductor is water-cooled with a 10 mm \times 10 mm cross section from the International Annealed Copper Standard (IACS), consisting of 100 % Cu. Turn-to-turn insulation is provided by 0.5 mm thickness double Dacron® glass, and 1 mm thickness of additional fiberglass insulation. Each coil is composed of stacks of four pancakes encapsulated with vacuum impregnated clear epoxy resin. The resulting dimensions for a single coil

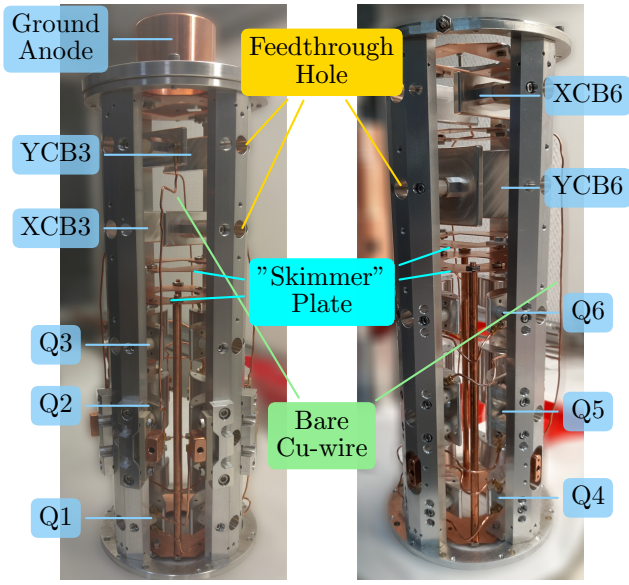


FIG. 4. Ion optics “boxes” used in the upgraded β -NQR beamline. Feedthrough holes allow BeCu extension posts connecting the UHV feedthroughs to the HV electrodes (see also details in fig. 2). The “skimmer” plates are grounded electrodes with apertures used to limit the effective length of the ion optics. Also shown are the stripped bare Cu wires used to connect electrodes in parallel to the common UHV feedthroughs. Left: Ion optics box upstream of the low-parallel-field sample position, containing the first quadrupole triplet and steerer assemblies. Right: Ion optics box for the high-parallel-field section, containing the second quadrupole triplet and steerer assemblies. Note that the beam enters from the bottom side of the image.

are shown in fig. 5, with a separation distance (between inner face of each coil) of 154.9 mm. The specified coils are sourced from Stangenes Industries Inc. (Palo Alto, CA).

The magnetic fields along the coil pair axis (i.e., the parallel fields on the sample) and along the beamline axis were calculated using the finite element method (FEM) software OPERA-3d (TOSCA Solver for Static Current Flow problems).³⁵ The simulated magnetic field homogeneity parallel to the sample surface (along the coil pair axis) and fringe fields along the beam axis are shown in fig. 6. The power supply provides up to 600 A at 50 V and is specified to have a stability of 0.01% ripple (60 mA rms) with a digital resolution of 16-bit at 200 mT. The power supply is sourced from Alpha Scientific Electronic (Stanton, CA) and installed with a water cooling system. Remote control of the power supply is available through an EPICS interface.^{32,33} A photograph of the magnet installed around the cryostat is shown in fig. 7. The cryostat is biased at the platform voltage and the copper electrode to the right of center is the grounded anode defining the deceleration gap.

Cryostat Modification

The existing cold-finger cryostat was modified to allow application of HV bias for the four-sector electrode which is mounted on the cryostat radiation shields via SHAPALTM

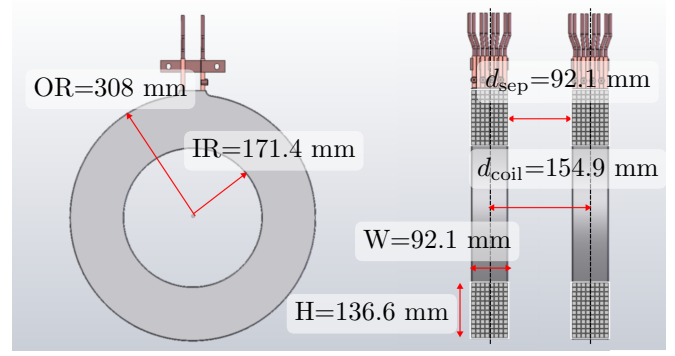


FIG. 5. Dimensions of the β -NQR modified Helmholtz coils. Left: Inner radius (IR) and outer radius (OR) of a single coil in the high-parallel-field magnet installed at the sample 2 position. Also shown are the cooling channel tails at the top of the model. Right: The dimensions of the coil pair, modified from a Helmholtz configuration to fit the UHV spectrometer chamber (with d_{coil} as the central separation and d_{sep} as the inner face separation between the coil pair). The width (W) and height (H) are the overall dimensions of the cross-section of the conductor turns.

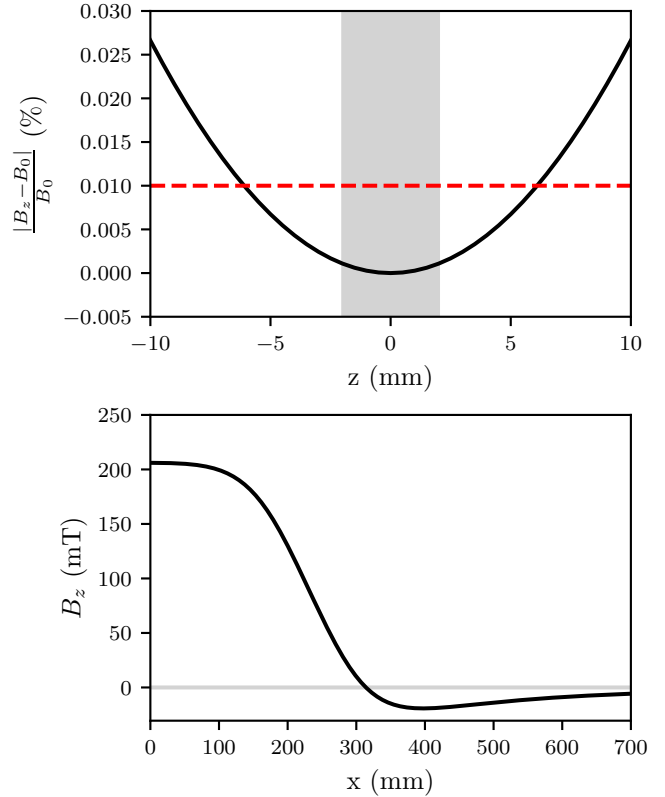


FIG. 6. Top: Relative field variation along the Helmholtz coil axis (i.e., across the sample) obtained by summing the measured field profile of a single coil. The sample is centered at $z = 0$ mm, where the uniformity of the applied field (206 mT here) is maximal. The red dashed line indicates the required field uniformity across the typical FWHM of the beam spot (grey shaded area). Bottom: Calculated stray fields (transverse to the beam momentum and parallel to sample surface) along the beamline axis (i.e., the x -axis) from FEM simulation. The sample is located at the $x = 0$ mm.

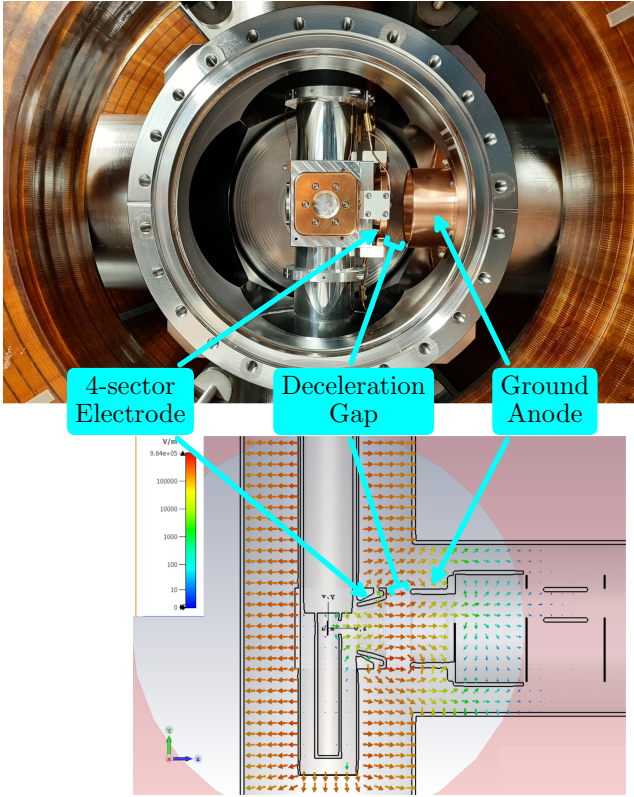


FIG. 7. Top: View of the β -NQR spectrometer through one of the beamline viewports with the stainless steel detector window removed. Note that the beam enters from the right side of the image. Shown here are the cryostat, the four-sector electrode (mounted on the cryostat heat-shield) and the 200 mT Helmholtz coil. Bottom: Calculated electric fields (using CST Studio)³⁶ with 10 kV bias applied to the sample (and the cryostat). The beam is decelerated to the desired implantation energy within a small (~ 21 mm) gap between the ground anode and the four-sector electrode.

Hi-M soft spacers, the latter providing electrical isolation while maintaining high thermal conductivity. The cryostat and the HV power supply for the four-sector steerers are housed inside the existing electrically isolated HV platform (via a ceramic vacuum break) to allow HV bias for beam deceleration. UHV compatible wires, such as Kapton insulated coaxial cables and oxygen-free high thermal conductivity (OFHC) bare copper wires, and lead-free solder joints are used for the assembly. Non-magnetic components such as connectors and fasteners are also used in the vicinity of the sample.

To accommodate for thermal contraction during low temperature measurements, the cryostat is supported on motorized bellows, which can be used to adjust the vertical alignment of the sample. In practice, the alignment is done by using the CCD camera at lower temperature to determine the current position and compare to a reference image with optimal alignment (usually determined at room temperature). The existing HV platform is also modified to accommodate a new support structure for the cryostat.

A continuous flow of liquid helium (LHe) can be provided

via a portable LHe dewar, which is installed onto the HV platform prior to the experiment. Operating temperatures between 4.5–300 K are routinely achievable. Two temperature sensors (GaAlAs diodes from Lake Shore Cryotronics, Inc.) are mounted on the side of an Al ring that holds the sample ladder. An additional platinum sensor (Pt-100 from Lake Shore Cryotronics, Inc.) is also installed on the heat shield. The temperature is controlled by adjusting the LHe transfer line needle valve, the He vapor mass flow to a roughing pump at the exhaust port of the cryostat, and the heater current for the cryostat (the latter is shown in fig. 8). Temperature stability is achieved with a Lake Shore model 336 controller driving a resistive heater on the cryostat cold block. Operating at colder sample temperatures (< 3 K) is foreseen in the near future with the addition of a cryo-head to be connected to the radiation shield. Measurements at even lower temperatures are planned in the future with the addition of a He-3 cryostat.

Detector System

Two scintillator telescope pairs (two on the left and two on the right of the cryostat position) are used to “view” the sample through thin (0.05 mm) stainless steel windows. The scintillator pairs are spaced sufficiently far apart to define a solid angle accepting β s originating at the sample, but rejecting most cosmic events and any β s from ions stopped in nearby parts. For the high-parallel-field spectrometer, Hamamatsu H6153-01 fine mesh dynode type photomultiplier tubes (PMTs) are used, as they are more resistant to the relatively high magnetic fields used during the experiments. The detector assembly, consisting of the scintillator (Saint-Gobain BC412 plastic scintillator with dimensions of 10 cm \times 10 cm \times 0.3 cm), Lucite light-guide, and the PMTs mounted in single steel tubes that provide limited magnetic shielding, are shown in fig. 9.

IV. COMMISSIONING AND FIRST RESULTS

As part of the instrument’s commissioning, all devices, including their control interfaces and interlock logic, are tested without beam to establish that functional requirements are met. *In operando* tests using ion beams are organized into stable beam tests using light ions (e.g., $^7\text{Li}^+$ and $^{12}\text{C}^+$) at 20 keV and RIB tests using $^8\text{Li}^+$ at 20 keV. The stable beam tests are done to check that the optics (i.e., quadrupoles, steerers, etc.) are manipulating the beam as expected. The RIB is used to further check functionality, such as the final beam spot at the sample in order to confirm the optics and to check the detectors and data acquisition (DAQ) system. The Helmholtz coil field strength and direction are checked with a hand held probe (Gauss meter). A final confirmation is done by using polarized ^8Li beam and using the β -NQR signal to directly measure the magnetic field on the sample (as described below).

There are two basic types of β -NMR measurements: resonance and relaxation. The beam commissioning with RIB employed both methods to check the full functionality of the equipment. A resonance measurement seeks to find the fre-

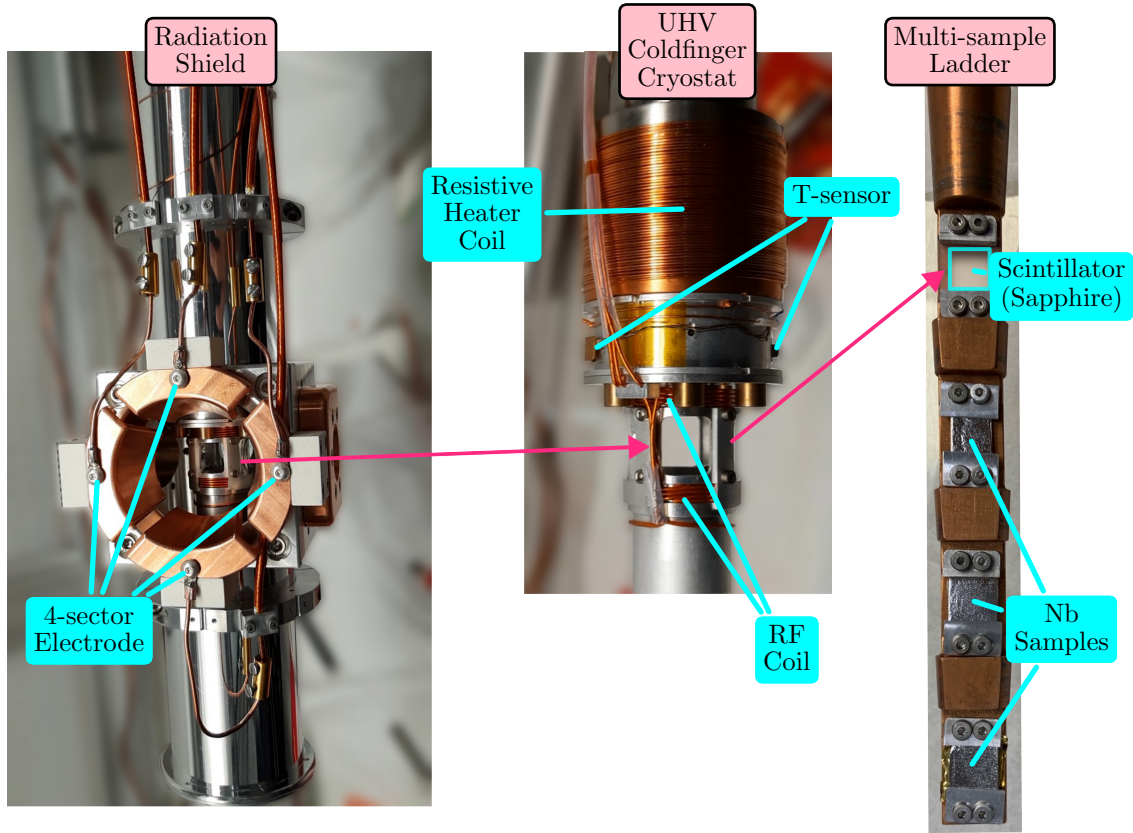


FIG. 8. Left: Radiation shield of the β -NQR cryostat with the four-sector electrode shown facing towards the incoming beam. Middle: Sample environment inside of the cryostat (with the radiation shield removed). Right: The sample ladder which is used to mount up to four samples via a UHV load-lock. The first position of the sample ladder in the photo is reserved for a sapphire scintillator, used for beam imaging using a CCD camera. The cyan-colored border indicates a 8 mm \times 8 mm viewing window of the CCD camera through the back of the sample ladder..

quency (i.e., the resonance condition) that corresponds to an energy difference between a pair of the probe's magnetic sub-levels. At TRIUMF, resonances are performed (predominantly) using continuous beam delivery and a transverse continuous wave (CW) RF field B_1 to manipulate the probe spins. In the CW approach, the RF field is stepped slowly through a range of frequencies close to the probe's Larmor frequency:

$$\nu_0 = \frac{\omega_0}{2\pi} = \frac{\gamma}{2\pi} B_0, \quad (4)$$

where $\gamma/(2\pi) = 6.302\,21(7)$ MHz/T³⁷ is the ^8Li gyromagnetic ratio and B_0 is the applied magnetic field. On resonance, in the limit of sufficiently large B_1 , the populations of the sub-levels involved in the transition(s) become equalized, resulting in a reduction in spin-polarization (or asymmetry).

In a relaxation measurement, the temporal evolution of the probe's spin polarization (which is initially very far from thermal equilibrium) is monitored as it returns to thermal equilibrium. The most commonly used type of such measurements is a so-called spin-lattice relaxation (SLR) measurement, wherein the applied field is parallel to the initial spin-polarization direction. Spin-polarization of the probe is lost through an energy exchange with its surrounding environment (often called the

"lattice" in NMR literature).³⁸ That is, spontaneous, stochastic fluctuations in the local field that are transverse to the probe spin direction serve to "reorient" it back to thermal equilibrium. Real time data for either mode can be conveniently displayed during the running experiment and analyzed using specialized β -NMR analysis software such as bfit.^{39,40}

The following calibration measurements were used to check the functionality of the detector, new Helmholtz coil, and the DAQ system. The magnetic field of the new coil on the sample location was precisely measured using the ^8Li resonance (see above description). A 99.99% pure Au foil (Alfa Aesar) was chosen as the calibration sample due to its relatively narrow resonance line and slow spin-lattice relaxation rate down to very low magnetic fields.^{41,42} The measured magnetic field on the Au foil can be obtained from the frequency of the resonant peak, ν_0 (eq. 4), as a function of the current in the Helmholtz coil. The results are shown in fig. 10, demonstrating a linear relation between the applied current and the measured magnetic fields, as expected. For this calibration, stray fields originating from the superconducting solenoid at the β -NMR leg (operated at 2.2 T during calibration measurements) contribute to a small constant background field.

During commissioning with RIB, various tunes (ion optics

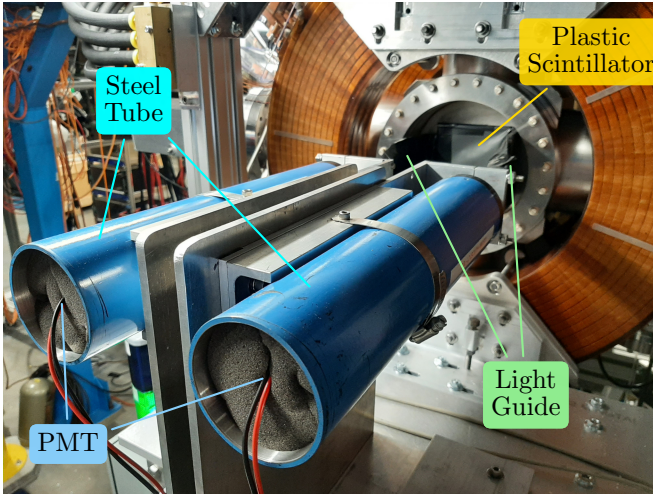


FIG. 9. The detector assembly, consisting of the BC412 plastic scintillator, Lucite light-guide, and the PMTs (mounted in single steel tubes) on their mechanical support.

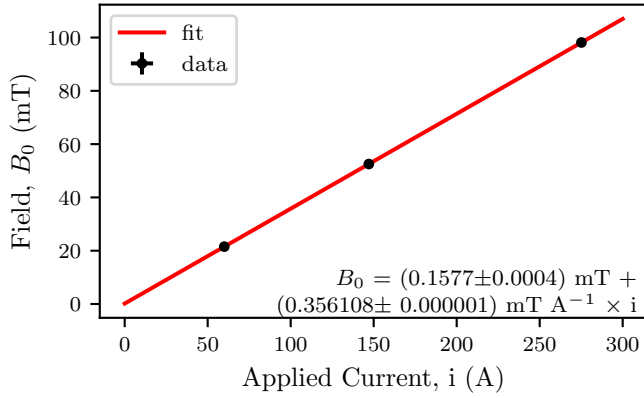


FIG. 10. Calibration of the high-parallel-field coil via the ^8Li NMR frequency in Au foil at different currents applied to the Helmholtz coils. The solid red line denotes a linear fit to the data, whose expression appears in the inset.

values along the beam path) at 20 keV $^8\text{Li}^+$ are established and their record is stored in a local database. These tunes can be re-scaled for different beam energies, applied magnetic fields, and RIBs, as well as re-loaded (i.e., as a starting condition) to speedup future beam delivery. An example of a typical beamspot image is shown in fig. 11, obtained at 200 mT using a 12.5 mm \times 12.5 mm sapphire plate at one of the sample positions on the sample ladder. The average transverse beamspot dimensions (i.e., FWHM) at the sample position for various applied magnetic fields are determined to be ~ 3 -4 mm.

Currently, spin-lattice relaxation (SLR) measurements on superconducting Nb samples have been successfully performed at several magnetic fields up to 200 mT. The SLR rate, commonly denoted as $1/T_1$, characterizes the time-constant in depolarization of the ^8Li nuclear spins after they are stopped inside the sample. The value of $1/T_1$ is extracted by fitting the measured time-dependent asymmetry $A(t)$ with a phenomenological depolarization function, e.g., $p(t, t'; 1/T_1) = \exp[-(t - t')/T_1]$ for a single exponential depolarization function, which is convolved with the square or rectangular beam pulse:

$$A(t) = A_0 \begin{cases} \frac{R_0 \int_0^t \exp[-(t - t')/\tau] p(t, t'; 1/T_1) dt'}{N(t)} & \text{for } t \leq \Delta, \\ \frac{R_0 \int_0^\Delta \exp[-(t - t')/\tau] p(t, t'; 1/T_1) dt'}{N(\Delta)} & \text{for } t > \Delta, \end{cases} \quad (5)$$

where Δ is the beam pulse length (typically ~ 1 -4 s), τ is the ^8Li lifetime, and $N(t)$ is the total count rate as defined earlier in eq. 2. Fig. 12 shows a typical asymmetry spectrum and its fit to eq. 5, measured on a residual resistivity ratio (RRR) ~ 300 Nb sample (cut, etched, and annealed at 1400 $^\circ\text{C}$) at 5 K using a 4 keV $^8\text{Li}^+$ beam. Applications are available to display the raw counts, the calculated asymmetry, and a fit to various depolarization functions during the experiment.^{39,40}

At applied magnetic fields below ~ 1 T, the dominant relaxation mechanism in Nb is due to cross relaxation between the ^8Li and the 100% abundant host ^{93}Nb nuclear spins,⁴³ which gives a Lorentzian dependence of $1/T_1$ on the local magnetic field according to:

$$\frac{1}{T_1} \approx \frac{(\gamma B_d)^2 \cdot (1/\tau_c)}{(1/\tau_c)^2 + [\gamma B_{\text{loc}}]^2}, \quad (6)$$

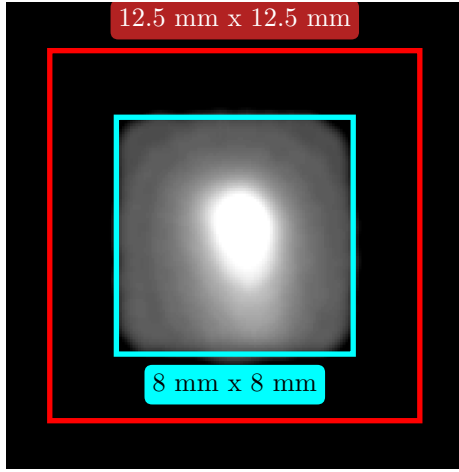


FIG. 11. Beamspot obtained at 200 mT on a sapphire scintillator. The image shown is looking upstream from the back side of the scintillator, viewed using the downstream CCD camera mounted on a viewport. The small (cyan) bounding box corresponds to the dimension of the visible area of the sapphire from the aperture at back of the sample ladder (see fig. 8), while the larger (red) box indicates the real size of the scintillator.

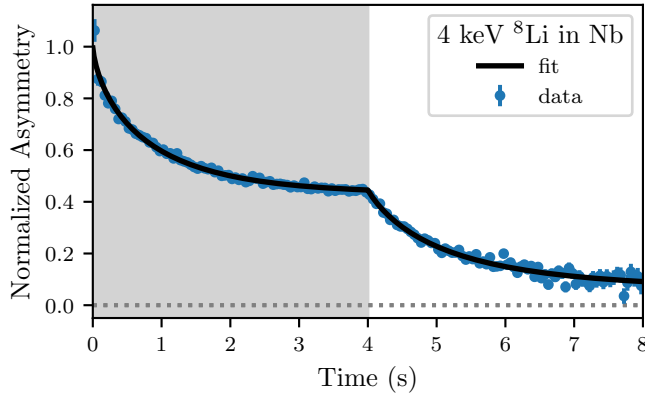


FIG. 12. ^8Li SLR normalized asymmetry spectrum, i.e., $A(t=0) = 1$, measured at 4.3 K and 200 mT applied field on a Nb sample using 4 s beam pulses of 4 keV $^8\text{Li}^+$. The shaded area indicates the measured asymmetry during beam pulse on. The solid line is the normalized fit to eq. 5.

where γ is the aforementioned ^8Li gyromagnetic ratio, B_{loc} is the measured local magnetic field, B_d is the magnitude of the fluctuating dipolar field (due to the host ^{93}Nb nuclear spins), and τ_c is the correlation time for the fluctuation in B_d . The variation of magnetic fields in the superconducting Nb due to Meissner screening can therefore be measured from the asymmetry spectra at different implantation energies (which corresponds to different implantation depths). Experimental results on the same sample shown in fig. 12 for five different implantation energies are shown in fig. 13. Here, a Nb sample is probed by ^8Li at five different depth distributions corresponding to ion energies of 4, 8, 12, 16 and 20 keV and average depths of 12, 22.5, 33, 44, 55 nm, respectively. The average depths are computed using the Stopping and Range

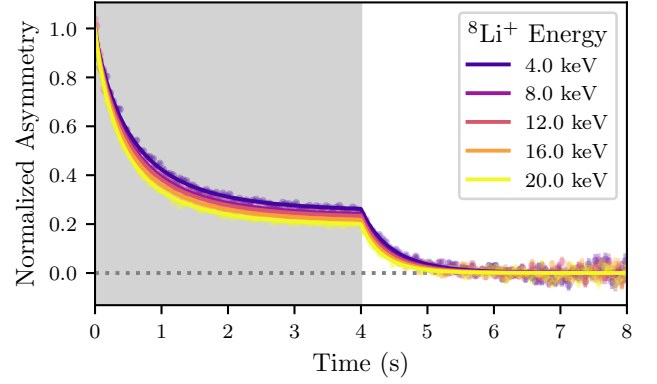


FIG. 13. Normalized fits to the SLR asymmetry spectra, i.e., $A(t=0) = 1$, of a Nb sample (RRR \sim 300) at various implantation energies measured at 4.5 K and at 98 mT. The higher relaxation rates deeper below the surface reflects the reduced magnetic field due to Meissner screening.

of Ions in Matter (SRIM) package.⁴⁴ The data set shows the expected signature of Meissner screening in superconducting Nb⁴⁵ as the depolarization rate increases as the ion is implanted deeper into the surface. Obtaining the accurate values of the local magnetic field requires a detailed analysis, taking into account the implantation distribution of the $^8\text{Li}^+$ ions at various energies, which averages over fields at different depths. The details of this analysis will be reported in a separate publication.

V. SCIENTIFIC APPLICATIONS & FUTURE CAPABILITIES

Just like conventional NMR using stable nuclei, the breadth of applications of β -NMR is enormous.^{21–24} The ability to operate at intermediate magnetic fields (10s to 100s of mT) opens new opportunities for scientific applications. In addition to the SRF material investigations, some of the experiments enabled in this field regime are: studies of thermally activated dynamics (i.e., moving the Bloembergen-Purcell-Pound peak⁴⁶ via adjusting B_0),^{47–51} and the study in soft condensed matter applications (see e.g.,^{52–54}) where the previously measured signal was completely wiped out below \sim 24 mT, but access to fields an order of magnitude higher may ameliorate this difficulty.

Recent measurements on Nb samples indicate vortex penetration at applied fields of 98 mT when Nb samples are warmed close to critical temperature (T_c). The mixed superconducting state is therefore also accessible and could be of interest for fundamental studies related to the superconducting vortex motion and dissipation.⁵⁵ β -NMR studies of the vortex lattice have been carried out in other superconductor materials such as $\text{YBa}_2\text{Cu}_3\text{O}_{7-\delta}$ ^{56,57} and NbSe_2 ⁵⁸ using β -NMR spectrometer (with out-of-plane applied fields). Further studies for SRF applications will benefit from lower sample temperatures in order to maintain the Meissner state at higher applied magnetic fields. Installation of a procured cryocooler is ongoing and measurements of superconducting samples in this regime are

expected in the near future.

VI. SUMMARY

The instrumentation at TRIUMF's β -NMR facility allows for the depth-dependent characterization of the local magnetic field near the surface of a sample. Both the infrastructure and instrumentation have been upgraded with a new beamline extension on the β -NQR leg, which has expanded previous capabilities from a maximum parallel magnetic field of 24 mT to 200 mT. This capability is targeted at testing SRF samples in a regime analogous to the magnetic field conditions in a Nb cavity operating at the fundamental limit, but will be widely useful to other condensed matter research. This capability is unique in the world and we anticipate additional use for other material science investigations.

ACKNOWLEDGMENTS

We thank: L. Merminga for involvement in the early stages of the project; M. H. Dehn for assistance during the beamline assembly; M. Cervantes for sample preparation; D. Lang, J. Keir, R. Abasalti, B. Hitti, B. Smith, D. Vyas, T. Au, J. Chow, T. Hruskovec, N. Muller, and M. Marchetto for providing excellent technical support. The hardware was funded through a Research Tools and Infrastructure grant from NSERC.

AUTHOR DECLARATIONS

Conflict of Interest

The authors have no conflicts to disclose.

Author Contributions

Edward Thoeng: Data Curation (equal); Formal Analysis (equal); Investigation (equal); Validation (equal); Visualization (equal); Writing — Original Draft Preparation (lead); Writing — Review & Editing (equal). **Ryan M. L. McFadden:** Data Curation (equal); Formal Analysis (equal); Investigation (supporting); Visualization (equal); Writing — Review & Editing (equal). **Suresh Saminathan:** Investigation (supporting); Methodology (equal); Validation (equal); Visualization (supporting). **Gerald D. Morris:** Conceptualization (equal); Investigation (equal); Project Administration (supporting); Resources (equal); Supervision (supporting); Validation (equal). **Philipp Kolb:** Investigation (equal); Project Administration (supporting); Supervision (supporting) Validation (equal). **Ben Matheson:** Methodology (equal); Visualization (supporting). **Md Asaduzzaman:** Investigation (supporting). **Richard Baartman:** Conceptualization (equal); Supervision (supporting). **Sarah R. Dunsiger:** Investigation (supporting). **Derek Fujimoto:** Formal Analysis (supporting); Investigation (supporting). **Tobias Junginger:** Formal

Analysis (supporting); Investigation (supporting); Project Administration (supporting); Supervision (supporting). **Victoria L. Karner:** Investigation (supporting). **Spencer Kiy:** Data Curation (equal); Investigation (supporting). **Ruohong Li:** Resources (equal). **Monika Stachura:** Investigation (supporting). **John O. Ticknor:** Investigation (supporting). **Robert F. Kieff:** Conceptualization (equal); Funding Acquisition (supporting). **W. Andrew MacFarlane:** Investigation (supporting); Supervision (supporting). **Robert E. Laxdal:** Conceptualization (equal); Formal Analysis (supporting); Funding Acquisition (lead); Project Administration (lead); Supervision (lead); Writing — Review & Editing (equal).

DATA AVAILABILITY STATEMENT

The data that support the findings of this study are available from the corresponding author upon reasonable request. Raw data of the β -NMR experiments are available for download from: <https://cmms.triumf.ca/>

- ¹H. Padamsee, "Future Prospects of Superconducting RF for Accelerator Applications," *Rev. Accel. Sci. Technol.* **10**, 125–156 (2019).
- ²H. Padamsee, "50 years of success for SRF accelerators—a review," *Supercond. Sci. Technol.* **30**, 053003 (2017).
- ³A. Gurevich, "Theory of RF superconductivity for resonant cavities," *Supercond. Sci. Technol.* **30**, 034004 (2017).
- ⁴G. Ciovati, "Effect of low-temperature baking on the radio-frequency properties of niobium superconducting cavities for particle accelerators," *J. Appl. Phys.* **96**, 1591–1600 (2004).
- ⁵F. He, W. Pan, P. Sha, J. Zhai, Z. Mi, X. Dai, S. Jin, Z. Zhang, C. Dong, B. Liu, H. Zhao, R. Ge, J. Zhao, Z. Mu, L. Du, L. Sun, L. Zhang, C. Yang, and X. Zheng, "Medium-temperature furnace baking of 1.3 GHz 9-cell superconducting cavities at IHEP," *Supercond. Sci. Technol.* **34**, 095005 (2021).
- ⁶H. Ito, H. Araki, K. Takahashi, and K. Umemori, "Influence of furnace baking on Q-E behavior of superconducting accelerating cavities," *Prog. Theor. Exp. Phys.* **2021** (2021), 10.1093/ptep/ptab056, 071G01.
- ⁷E. M. Lechner, J. W. Angle, F. A. Stevie, M. J. Kelley, C. E. Reece, and A. D. Palczewski, "Rf surface resistance tuning of superconducting niobium via thermal diffusion of native oxide," *Appl. Phys. Lett.* **119**, 082601 (2021).
- ⁸A. Grassellino, A. Romanenko, D. Sergatskov, O. Melnychuk, Y. Trenikhina, A. Crawford, A. Rowe, M. Wong, T. Khabiboulline, and F. Barkov, "Nitrogen and argon doping of niobium for superconducting radio frequency cavities: a pathway to highly efficient accelerating structures," *Supercond. Sci. Technol.* **26**, 102001 (2013).
- ⁹A. Grassellino, A. Romanenko, Y. Trenikhina, M. Checchin, M. Martinello, O. S. Melnychuk, S. Chandrasekaran, D. A. Sergatskov, S. Posen, A. C. Crawford, S. Aderhold, and D. Bice, "Unprecedented quality factors at accelerating gradients up to 45 MVm⁻¹ in niobium superconducting resonators via low temperature nitrogen infusion," *Supercond. Sci. Technol.* **30**, 094004 (2017).
- ¹⁰T. Kubo, "Multilayer coating for higher accelerating fields in superconducting radio-frequency cavities: a review of theoretical aspects," *Supercond. Sci. Technol.* **30**, 023001 (2016).
- ¹¹A. Gurevich, "Enhancement of rf breakdown field of superconductors by multilayer coating," *Appl. Phys. Lett.* **88**, 012511 (2006).
- ¹²A. Gurevich, "Maximum screening fields of superconducting multilayer structures," *AIP Advances* **5**, 017112 (2015).
- ¹³S. Posen, M. K. Transtrum, G. Catelani, M. U. Liepe, and J. P. Sethna, "Shielding Superconductors with Thin Films as Applied to rf Cavities for Particle Accelerators," *Phys. Rev. Applied* **4**, 044019 (2015).
- ¹⁴M. Checchin, A. Grassellino, M. Martinello, S. Posen, A. Romanenko, and J. Zasadzinski, "Ultimate Gradient Limitation in Niobium Superconducting Accelerating Cavities," in *Proc. of International Particle Accelerator Conference (IPAC'16), Busan, Korea, May 8-13, 2016*, International Particle

- Accelerator Conference No. 7 (JACoW, Geneva, Switzerland, 2016) pp. 2254–2257, doi:10.18429/JACoW-IPAC2016-WEPMR002.
- ¹⁵T. Junginger, S. H. Abidi, R. D. Maffett, T. Buck, M. H. Dehn, S. Gheidi, R. Kiefl, P. Kolb, D. Storey, E. Thoeng, W. Wasserman, and R. E. Laxdal, “Field of first magnetic flux entry and pinning strength of superconductors for rf application measured with muon spin rotation,” *Phys. Rev. Accel. Beams* **21**, 032002 (2018).
 - ¹⁶A. Grassellino, C. Beard, P. Kolb, R. Laxdal, N. S. Lockyer, D. Longuevergne, and J. E. Sonier, “Muon spin rotation studies of niobium for superconducting rf applications,” *Phys. Rev. ST Accel. Beams* **16**, 062002 (2013).
 - ¹⁷R. Laxdal, S. Abidi, T. Buck, T. Junginger, R. Kiefl, P. Kolb, Y. Ma, L. Yang, and Z. Yao, “Characterization of SRF Materials at the TRIUMF muSR Facility,” in *17th International Conference on RF Superconductivity* (2015) p. MOPB050.
 - ¹⁸Z. Salman, T. Prokscha, P. Keller, E. Morenzoni, H. Saadaoui, K. Sedlak, T. Shiroka, S. Sidorov, A. Suter, V. Vrankovic, and H.-P. Weber, “Design and simulation of a spin rotator for longitudinal field measurements in the low energy muons spectrometer,” *Physics Procedia* **30**, 55–60 (2012), 12th International Conference on Muon Spin Rotation, Relaxation and Resonance (μ SR2011).
 - ¹⁹T. Prokscha, E. Morenzoni, K. Deiters, F. Foroughi, D. George, R. Kobler, A. Suter, and V. Vrankovic, “The new μ E4 beam at PSI: A hybrid-type large acceptance channel for the generation of a high intensity surface-muon beam,” *Nucl. Instrum. Methods Phys. Res., Sect. A* **595**, 317–331 (2008).
 - ²⁰E. Morenzoni, H. Glückler, T. Prokscha, H. Weber, E. Forgan, T. Jackson, H. Luetkens, C. Niedermayer, M. Pleines, M. Birke, A. Hofer, J. Litterst, T. Riseman, and G. Schatz, “Low-energy μ SR at PSI: present and future,” *Physica B* **289–290**, 653–657 (2000).
 - ²¹W. A. MacFarlane, “Status and progress of ion-implanted β NMR at triumf,” *Z. Phys. Chem.* **236**, 757–798 (2022).
 - ²²W. A. MacFarlane, “Implanted-ion β NMR: A new probe for nanoscience,” *Solid State Nucl. Magn. Reson.* **68–69**, 1–12 (2015).
 - ²³G. D. Morris, “ β -NMR,” *Hyperfine Interact.* **225**, 173–182 (2014).
 - ²⁴S. R. Kreitzman and G. D. Morris, “TRIUMF MuSR and β NMR research facilities,” *JPS Conf. Proc.* **21**, 011056 (2018).
 - ²⁵X. Fléhard, E. Liénard, O. Naviliat-Cuncic, D. Rodríguez, M. A. G. Alvarez, G. Ban, B. Carniol, D. Etasse, J. M. Fontbonne, A. M. Lallena, and J. Praena, “Measurement of the ^8Li half-life,” *Phys. Rev. C* **82**, 027309 (2010).
 - ²⁶J. Dilling and R. Krücken, “The experimental facilities at ISAC,” *Hyperfine Interact.* **225**, 111–114 (2014).
 - ²⁷C. D. P. Levy, M. R. Pearson, R. F. Kiefl, E. Mané, G. D. Morris, and A. Voss, “Laser polarization facility,” *Hyperfine Interact.* **225**, 165–172 (2014).
 - ²⁸W. A. MacFarlane, C. D. P. Levy, M. R. Pearson, T. Buck, K. H. Chow, A. N. Hariwal, R. F. Kiefl, F. H. McGee, G. D. Morris, and D. Wang, “The Initial State of Optically Polarized $^8\text{Li}^+$ from the β -NMR in Bismuth,” *J. Phys. Conf. Ser.* **551**, 012059 (2014).
 - ²⁹GPT, “General particle tracer,” .
 - ³⁰E. Heighway and R. Hutcheon, “Transoptr — a second order beam transport design code with optimization and constraints,” *Nucl. Instrum. Methods Phys. Res.* **187**, 89–95 (1981).
 - ³¹R. Baartman, *TRANSOPTR Reference Manual*, TRIUMF (2022).
 - ³²L. R. Dalesio, J. O. Hill, M. Kraimer, S. Lewis, D. Murray, S. Hunt, W. Watson, M. Clausen, and J. Dalesio, “The experimental physics and industrial control system architecture: past, present, and future,” *Nucl. Instrum. Methods Phys. Res., Sect. A* **352**, 179–184 (1994).
 - ³³EPICS, “Experimental physics and industrial control system,” <http://www.aps.anl.gov/epics/>.
 - ³⁴Z. Salman, K. H. Chow, M. D. Hossain, R. F. Kiefl, C. D. P. Levy, T. J. Parolin, M. R. Pearson, H. Saadaoui, D. Wang, and W. A. MacFarlane, “ β -detected nuclear quadrupole resonance and relaxation of $^8\text{Li}^+$ in sapphire,” *J. Phys. Conf. Ser.* **551**, 012034 (2014).
 - ³⁵OPERA, “Opera-3d,” .
 - ³⁶CST, “CST Studio,” .
 - ³⁷N. J. Stone, “Table of recommended nuclear magnetic dipole moments,” Tech. Rep. INDC(NDS)–0794 (International Atomic Energy Agency (IAEA), 2019).
 - ³⁸C. P. Slichter, “Spin-lattice relaxation and motional narrowing of resonance lines,” in *Principles of Magnetic Resonance* (Springer Berlin Heidelberg, Berlin, Heidelberg, 1990) pp. 145–218.
 - ³⁹D. Fujimoto, “Digging into mud with python: mudpy, bdata, and bfit,” (2020), [arXiv:2004.10395](https://arxiv.org/abs/2004.10395).
 - ⁴⁰D. Fujimoto, “bfit: A python application for beta-detected nmr,” *Journal of Open Source Software* **6**, 3598 (2021).
 - ⁴¹W. A. MacFarlane, K. H. Chow, M. D. Hossain, V. L. Karner, R. F. Kiefl, R. M. L. McFadden, G. D. Morris, H. Saadaoui, and Z. Salman, “The spin relaxation of $^8\text{Li}^+$ in gold at low magnetic field,” *JPS Conf. Proc.* **21**, 011020 (2018).
 - ⁴²T. J. Parolin, Z. Salman, K. H. Chow, Q. Song, J. Valiani, H. Saadaoui, A. O’Halloran, M. D. Hossain, T. A. Keeler, R. F. Kiefl, S. R. Kreitzman, C. D. P. Levy, R. I. Miller, G. D. Morris, M. R. Pearson, M. Smadella, D. Wang, M. Xu, and W. A. MacFarlane, “High resolution β -NMR study of $^8\text{Li}^+$ implanted in gold,” *Phys. Rev. B* **77**, 214107 (2008).
 - ⁴³T. J. Parolin, J. Shi, Z. Salman, K. H. Chow, P. Dosanjh, H. Saadaoui, Q. Song, M. D. Hossain, R. F. Kiefl, C. D. P. Levy, M. R. Pearson, and W. A. MacFarlane, “Nuclear magnetic resonance study of Li implanted in a thin film of niobium,” *Phys. Rev. B* **80**, 174109 (2009).
 - ⁴⁴J. F. Ziegler, M. D. Ziegler, and J. P. Biersack, “SRIM - The stopping and range of ions in matter (2010),” *Nucl. Instrum. Methods Phys. Res., Sect. B* **268**, 1818–1823 (2010).
 - ⁴⁵M. D. Hossain, Z. Salman, D. Wang, K. H. Chow, S. Kreitzman, T. A. Keeler, C. D. P. Levy, W. A. MacFarlane, R. I. Miller, G. D. Morris, T. J. Parolin, M. Pearson, H. Saadaoui, and R. F. Kiefl, “Low-field cross spin relaxation of ^8Li in superconducting NbSe_2 ,” *Phys. Rev. B* **79**, 144518 (2009).
 - ⁴⁶N. Bloembergen, E. M. Purcell, and R. V. Pound, “Relaxation effects in nuclear magnetic resonance absorption,” *Phys. Rev.* **73**, 679–712 (1948).
 - ⁴⁷I. McKenzie, M. Harada, R. F. Kiefl, C. D. P. Levy, W. A. MacFarlane, G. D. Morris, S.-I. Ogata, M. R. Pearson, and J. Sugiyama, “ β -NMR measurements of lithium ion transport in thin films of pure and lithium-salt-doped poly(ethylene oxide),” *J. Am. Chem. Soc.* **136**, 7833–7836 (2014).
 - ⁴⁸I. McKenzie, D. L. Cortie, M. Harada, R. F. Kiefl, C. D. P. Levy, W. A. MacFarlane, R. M. L. McFadden, G. D. Morris, S.-I. Ogata, M. R. Pearson, and J. Sugiyama, “ β -NMR measurements of molecular-scale lithium-ion dynamics in poly(ethylene oxide)-lithium-salt thin films,” *J. Chem. Phys.* **146**, 244903 (2017).
 - ⁴⁹R. M. L. McFadden, T. J. Buck, A. Chatzichristos, C.-C. Chen, K. H. Chow, D. L. Cortie, M. H. Dehn, V. L. Karner, D. Koumoulis, C. D. P. Levy, C. Li, I. McKenzie, R. Merkle, G. D. Morris, M. R. Pearson, Z. Salman, D. Samuelis, M. Stachura, J. Xiao, J. Maier, R. F. Kiefl, and W. A. MacFarlane, “Microscopic dynamics of Li^+ in rutile TiO_2 revealed by ^8Li β -detected nuclear magnetic resonance,” *Chem. Mater.* **29**, 10187–10197 (2017).
 - ⁵⁰R. M. L. McFadden, A. Chatzichristos, K. H. Chow, D. L. Cortie, M. H. Dehn, D. Fujimoto, M. D. Hossain, H. Ji, V. L. Karner, R. F. Kiefl, C. D. P. Levy, R. Li, I. McKenzie, G. D. Morris, O. Ofer, M. R. Pearson, M. Stachura, R. J. Cava, and W. A. MacFarlane, “Ionic and electronic properties of the topological insulator $\text{Bi}_2\text{Te}_3\text{Se}$ investigated via β -detected nuclear magnetic relaxation and resonance of ^8Li ,” *Phys. Rev. B* **99**, 125201 (2019).
 - ⁵¹R. M. L. McFadden, A. Chatzichristos, D. L. Cortie, D. Fujimoto, Y. S. Hor, H. Ji, V. L. Karner, R. F. Kiefl, C. D. P. Levy, R. Li, I. McKenzie, G. D. Morris, M. R. Pearson, M. Stachura, R. J. Cava, and W. A. MacFarlane, “Local electronic and magnetic properties of the doped topological insulators $\text{Bi}_2\text{Se}_3\text{:Ca}$ and $\text{Bi}_2\text{Te}_3\text{:Mn}$ investigated using ion-implanted ^8Li β -NMR,” *Phys. Rev. B* **102**, 235206 (2020).
 - ⁵²F. H. McGee, I. McKenzie, T. Buck, C. R. Daley, J. A. Forrest, M. Harada, R. F. Kiefl, C. D. P. Levy, G. D. Morris, M. R. Pearson, J. Sugiyama, D. Wang, and W. A. MacFarlane, “A brief survey of β -detected NMR of implanted $^8\text{Li}^+$ in organic polymers,” *J. Phys.: Conf. Ser.* **551**, 012039 (2014).
 - ⁵³I. McKenzie, C. R. Daley, R. F. Kiefl, C. D. P. Levy, W. A. MacFarlane, G. D. Morris, M. R. Pearson, D. Wang, and J. A. Forrest, “Enhanced high-frequency molecular dynamics in the near-surface region of polystyrene thin films observed with β -NMR,” *Soft Matter* **11**, 1755–1761 (2015).
 - ⁵⁴I. McKenzie, Y. Chai, D. L. Cortie, J. A. Forrest, D. Fujimoto, V. L. Karner, R. F. Kiefl, C. D. P. Levy, W. A. MacFarlane, R. M. L. McFadden, G. D. Morris, M. R. Pearson, and S. Zhu, “Direct measurements of the temperature, depth and processing dependence of phenyl ring dynamics in polystyrene thin films by β -detected NMR,” *Soft Matter* **14**, 7324–7334 (2018).
 - ⁵⁵S. Eley, A. Glatz, and R. Willa, “Challenges and transformative opportunities in superconductor vortex physics,” *J. Appl. Phys.* **130**, 050901 (2021).
 - ⁵⁶H. Saadaoui, W. MacFarlane, G. Morris, Z. Salman, K. Chow, I. Fan, M. Hossain, R. Liang, A. Mansour, T. Parolin, M. Smadella, Q. Song,

- D. Wang, and R. Kiefl, “Vortex lattice disorder in $\text{YBa}_2\text{Cu}_3\text{O}_{7-\delta}$ studied with β -nmr,” *Physica B* **404**, 730–733 (2009).
- ⁵⁷H. Saadaoui, W. A. MacFarlane, Z. Salman, G. D. Morris, Q. Song, K. H. Chow, M. D. Hossain, C. D. P. Levy, A. I. Mansour, T. J. Parolin, M. R. Pearson, M. Smadella, D. Wang, and R. F. Kiefl, “Vortex lattice disorder in $\text{YBa}_2\text{Cu}_3\text{O}_{7-\delta}$ probed using β -NMR,” *Phys. Rev. B* **80**, 224503 (2009).
- ⁵⁸Z. Salman, D. Wang, K. H. Chow, M. D. Hossain, S. R. Kreitzman, T. A. Keeler, C. D. P. Levy, W. A. MacFarlane, R. I. Miller, G. D. Morris, T. J. Parolin, H. Saadaoui, M. Smadella, and R. F. Kiefl, “Magnetic-field effects on the size of vortices below the surface of NbSe_2 detected using low energy β -nmr,” *Phys. Rev. Lett.* **98**, 167001 (2007).